QUANTUM RESERVOIR COMPUTING FOR EFFICIENT SIGNAL PROCESSING

Project Deliverable

D1.2 Quantitative model of defect-based QR

Lead Beneficiary:	Loughborough University
Author(s):	Viktor Ivády, Gerard McCaul
Contributor(s):	All consortium partners
Dissemination Level:	Public (PU)

https://www.qrc-4-esp.eu

Funded by
the European Union

QRC-4-ESP

Document History:

Version and date	Changes
1.0 - December 12, 2024	Initial version

DISCLAIMER:

Funded by the European Union. Views and opinions expressed are however those of the author(s) only and do not necessarily reflect those of the European Union or the European Commission. Neither the European Union nor the granting authority can be held responsible for them.

This document contains information which is proprietary to the QRC-4-ESP consortium. Neither this document nor the information contained herein shall be used, duplicated or communicated by any means to any third party, in whole or parts, except with the prior written consent of the QRC-4-ESP coordinator or partner on behalf of the project consortium.

Contents

1 Introduction **3**

2 Silicon Vacancy Model **3**
2.1 Structure and optical signature 3
2.2 Modelling the Vacancy 4
2.3 First principles determination of unmeasurable defect parameters . . . 6

3 Numerical Simulation **7**
3.1 Mathematica model 8
3.2 C++ implementation for HPC 8
3.3 Coherent optical drive, photoluminescence excitation spectrum, and optical spin initialization of the VSi center 9
3.4 Optically detected magnetic resonance simulation 10

4 Outlook **12**

1 Introduction

This report summarizes the first results of numerical modelling of point defect spin qubits for quantum reservoir computing. This includes the development of a versatile Mathematica package for easy-access modelling of different silicon-vacancy centres, and the parallel implementation of a model running on high-performance computing clusters for efficient parameter scanning. Numerical simulations in this work package rest on two pillars, 1) modelling and prototyping using a flexible and easily accessible Mathematica notebook implementing key equations for optically, microwave, and radio frequency driven coupled point defect and nuclear spin systems of varying dimensions, and 2) a message passing interface (MPI) parallelized C++ code for large scale parameter scanning carried out on high-performance computing infrastructures. The capabilities of the modelling and the numerical packages are demonstrated via the specific case of the negatively charged silicon-vacancy (V_{Si}) centre in 4H polytype of silicon carbide (4H-SiC). The V_{Si} centre, also known as the V1 and V2 color centres, feature desirable properties for performing reservoir computing, such as high spin-3/2 ground and excited state electron spin, a handful of coupled ^{13}C and ^{29}Si nuclear spins, and a narrow optical linewidth. This enables the resolution of spin state-dependent zero-phonon absorption and luminescence lines, and a route to scaling up a silicon vacancy-based reservoir via optical coupling to the defect. All these properties and capabilities make the silicon vacancy the primary target of our testing and developments.

The rest of this report is organized as follows. In Sec. 2, we briefly discuss the physics of the silicon vacancy, and the equations governing the optical and spin dynamics of driven centres. Sec. 3 details the development of two simulation packages, and outlines some of the numerical results derived from them. Finally, Sec. 4 outlines the future development of this work, and its integration into the broader QRC framework.

2 Silicon Vacancy Model

2.1 Structure and optical signature

When considering the microscopic structure of silicon vacancies in 4H-SiC, there are two variants. These are the so-called h and k silicon vacancies, illustrated in Fig. 1a, and correspond to the V1 and V2 photoluminescence lines, respectively. The two variants are qualitatively the same, featuring only minor quantitative differences, which in turn enlarges the available parameter space for QRC applications. The highly confined C3v symmetric electronic states of the defect are built up from four dangling bonds of the carbon atoms adjacent to the silicon vacancy site. In the negative charge state (which is stable at Fermi energies close to the middle of the band gap), the defect possesses spin-3/2 ground and optically excited states, shown in Fig. 1b. These can be optically resolved at low temperature with photoluminescence excitation (PLE) measurements, as shown in Fig. 2a. Due to a weak coupling to the local electric field and strain different VSi centres can exhibit slightly shifted, sometimes overlapping PLE spectra, see Fig. 2b. In addition to this, there exist optically inaccessible doublet excited states giving rise to a non-spin conserving, non-radiative decay pathway from the optically excited quartet excited state to the quartet ground state. The spin state resolved optical excitation and

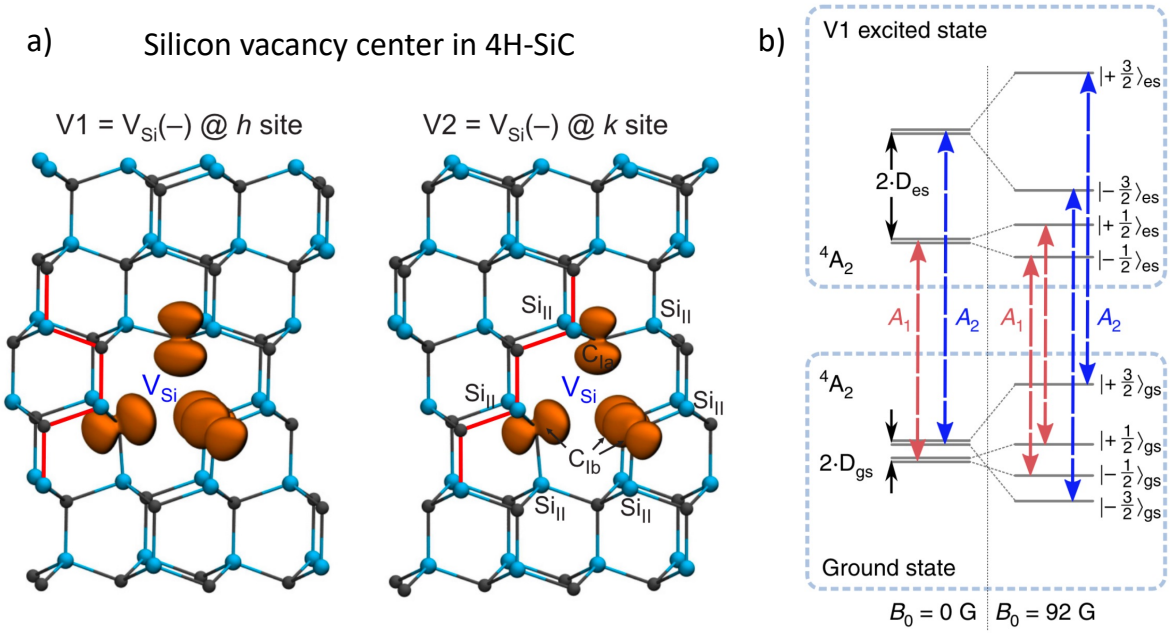

Figure 1: Structure and electronic structure of the negatively charged silicon-vacancy centre (V_{Si}) in 4H-SiC. a) The two variants of V_{Si} in 4H-SiC are the V1 and V2 centres. Orange lobs depict an isosurface of the spin density of the V1 and V2 centres. C_I and Si_{II} label the first and second neighbor carbon and silicon-vacancy of the in 4H-SiC. b) Schematic electronic and spin fine structure the ground and excited states of silicon vacancy. Transitions A_1 and A_2 of spin subspaces $m_S = \pm 1/2$ and $m_S = \pm 3/2$ can be resolved in photoluminescence Excitation measurements, see Fig. 2

the spin-non-conserving decay enables both high fidelity initialization and read out of the electron spin.

2.2 Modelling the Vacancy

With this setup, we now discuss the equations modelling these silicon vacancies, which form the core of the simulation packages. The electronic structure of N silicon vacancies in the rotating wave approximation (including the electron spin degrees of freedom can be written as

$$H_{\text{opt}}(t) = \sum_i^N \begin{bmatrix} \Delta_i(t) + D_i^{(e)}(S_z^2 - \frac{5}{4}) & \Omega(t) \\ \Omega(t) & D_i^{(g)}(S_z^2 - \frac{5}{4}) \end{bmatrix}, \tag{1}$$

where $\Delta_i(t)$ is the onsite detuning of the silicon vacancies (and can be either static or dynamic), $\Omega(t)$ is the time-dependent global coherent optical drive of the centres, and $D_i^{(e)}$ and $D_i^{(g)}$ are the excited and ground state zero field splitting values. The ground (excited) state values of the zero-field splitting $2D^{(g)}$ ($2D^{(e)}$) is 5 MHz (985 MHz) for the V1 centre and 70 MHz (1000 MHz) for the V2 centre.[1–3]

The propagation of the system's density matrix ρ under optical excitation and spin-

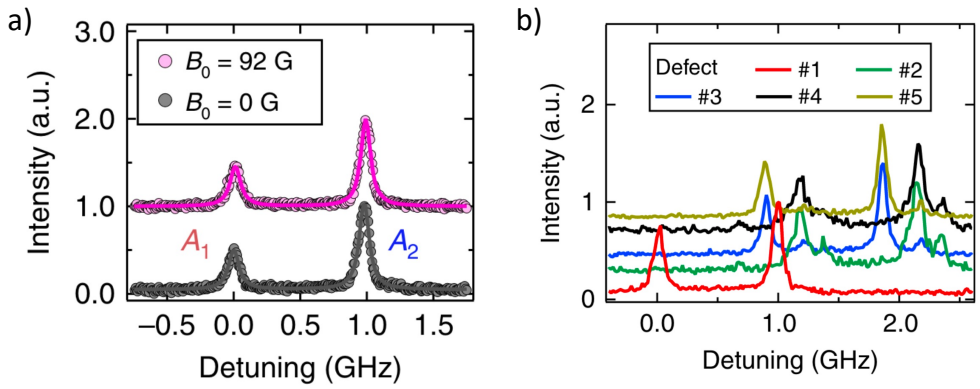

Figure 2: Photoluminescent excitation spectra of V1 centres in 4H-SiC. a) PLE at two magnetic fields showing negligible Zeemann shifts and b) five V1 centres in exhibiting different local detuning Δ_i.

selective non-radiative decay is described by

$$\frac{d\rho}{dt} = -\frac{i}{\hbar}[H_{\text{opt}}(t), \rho] + \sum_i \gamma_i \left(L_i \rho L_i^\dagger - \frac{1}{2}\{L_i^\dagger L_i, \rho\} \right), \tag{2}$$

where $\gamma_1 = 56.05$ MHz ($\gamma_2 = 24.4$ MHz)[4] specifies the rate of spin-conserving (spin-nonconserving) incoherent decay from excited states to the ground state. The corresponding jump operators L_i can be given as

$$L_1 = |\text{g}\rangle \langle \text{e}|, \tag{3}$$

and

$$L_2 = |\pm 1/2\rangle^{(\text{g})} \langle \pm 3/2|^{(\text{e})}. \tag{4}$$

Beyond this, the fine structure to the silicon vacancy electron spin states are governed by an additional two interactions. These consist of the zero-field spitting originating from the dipolar coupling of the three unpaired electron spins in the quartet state in C_{3v}, and the Zeeman interaction from the applied magnetic field. Due to the large spin and relatively low symmetry of the defect, higher-order Zeeman terms are allowed for the silicon-vacancy centre. The symmetry-motivated expression of the electron spin Hamiltonian can be found in ref.[5].

The resulting ground and excited state fine structures are depicted in Fig. 3a. At zero magnetic field, the $m_S = \pm 1/2$ and the $m_S = \pm 3/2$ subspaces are split by twice the zero-field splitting parameters D. By applying a magnetic field parallel to the symmetry axis of the defect, the states are further split due to the Zeeman interaction. The splitting is mostly linear at low magnetic fields. At specific positive magnetic fields a level crossing between the $m_S = -3/2$ and the $m_S = +1/2$ (as well as the $m_S = -3/2$ and the $m_S = -1/2$) enables coupling to environmental degrees of freedoms, such as nuclear spin. These regions are called the ground (exited) state-level avoiding crossing GSLAC-1 (ESLAC-1) and GSLAC-2 (ESLAC-2).

Applying either a continuous wave (CW) or pulsed microwave (MW) drive one can rotate the electron spin at resonance conditions giving rise to luminescence intensity changes through the spin-dependent optical signal of the centre. Such measurements are referred to as CW and pulsed optically detected magnetic resonance (ODMR). By

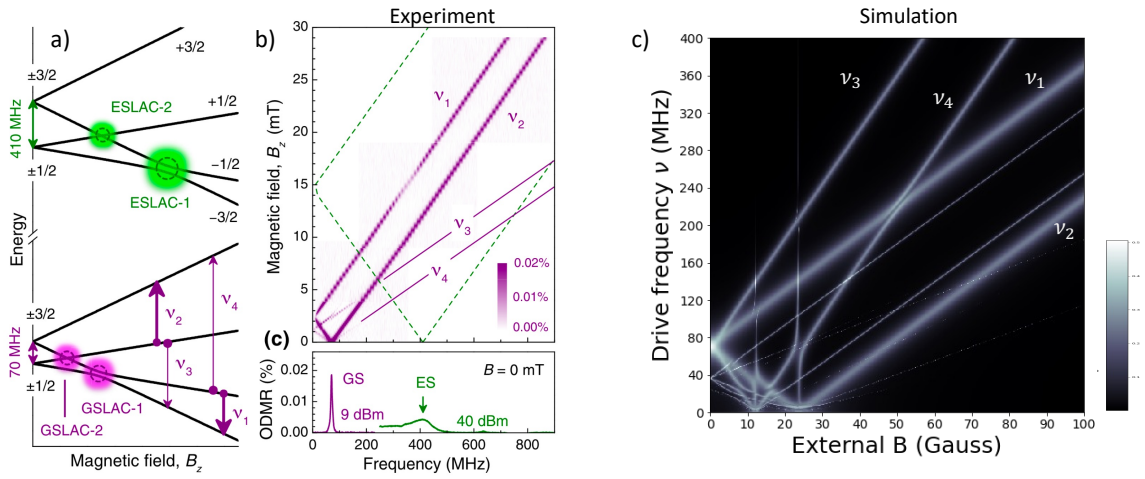

Figure 3: Simulated and measured ODMR map in the ground state of the V2 centre in 4H-SiC. a) schematic diagram of the energy fine structure at small magnetic fields, b) measured ODMR map revealing 4 transitions, c) high resolution simulated ODMR map of the silicon vacancy

scanning both the magnetic field parallel to the defect symmetry axis and the frequency of the applied MW drive, one can make an ODMR map by detecting the intensity of the defect's photoluminescent (PL) emission, as in Fig. 3b. This reveals the single and double quantum jump transitions between the states in Fig. 3a, with Double quantum jump transitions are enabled by a third order Zeeman term. Fig. 3c shows the simulated ODMR map of the silicon-vacancy centre, whose implementation is discussed in detail in section **??**.

2.3 First principles determination of unmeasurable defect parameters

The lattice of 4H-SiC contains 4.68% ^{29}Si and 1.07% ^{13}C in natural abundance. Coupling to nuclear spins gives rise to the hyperfine structure of the spin states resolvable in magnetic resonance techniques. In order to include nuclear spin in the description, we need to extend the spin Hamiltonian with the use of a hyperfine tensor coupling state defect states to nuclear spins. Given the potentially large number of coupled nuclear spins and their long coherence time, they are an ideal means of extending the lifetime of point defect-based quantum systems for quantum reservoir computing.

The hyperfine tensors specifying the coupling between nuclear and electron spins are a crucial component of quantitatively accurate modeling. They are however not generally accessible in experiments, especially for weakly coupled nuclear spins since such a characterization requires a tremendous amount of resources. Alternatively, first-principles calculations can be utilized to obtain all hyperfine tensors from the computed electron density of the defect.

A well-developed and reliable method to obtain these properties is via Density functional theory (DFT). Recent advances [6, 7] (including the preceeding work of the consortium partner ELTE) have allowed hyperfine tensors to be calculated with remarkable accuracy. This includes point defect spin qubits such as the NV centre in diamond and the V2 centre in 4H-SiC [7]. Using these developments, it is possible to employ DFT

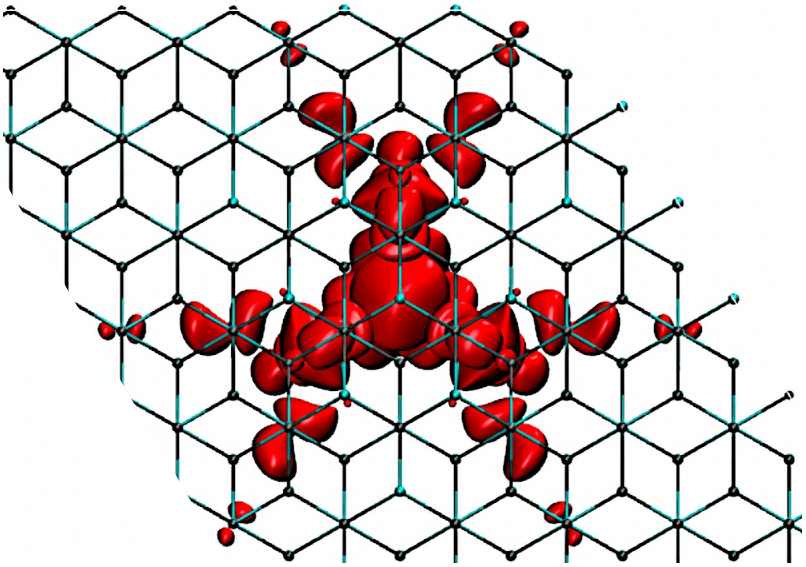

Figure 4: Spatial distribution of the spin density of the silicon vacancy in 4H-SiC. Black and cyan balls represent silicon and carbon atoms, while red lobes depict the isosurface of the electron spin density.

to map the spin density distribution of the silicon vacancy, as depicted in Fig.4 Taken together, these developments permit the calculation of hyperfine tensors by employing underlying DFT calculations.

Utilizing this state-of-the-art methodology and large 1536-atom supercell model with HSE06 hybrid functional calculations, we have calculated hyperfine tensors for the V1 silicon vacancy defect in the reporting period. Hyperfine tensors calculated for ≈6000 atomic sites are now available online at https://ivadygroup.elte.hu/hyperfine/.

Having all the terms and parameters of the model Hamiltonian set we can carry out predictive numerical simulations.

3 Numerical Simulation

There are two distinct ways in which computer simulations can contribute to the realization of point defect-based quantum reservoir computing (QRC), as illustrated in Sec. 4 via Fig. 9.

First, simulations can assist in selecting input and output parameters. Depending on the choices made, varying levels of complexity may need to be incorporated into the simulations. These complexities could include factors such as the number of silicon vacancy defects, the number of electronic states per defect (e.g., ground and excited states), nuclear spin degrees of freedom, and the characteristics of external drives, such as static or time-dependent electric and magnetic fields. Given the wide range of possibilities, it is essential to have an accessible and highly configurable simulation package that facilitates rapid prototyping. To address this need, we first developed a flexible model in Wolfram Mathematica that is available to all consortium partners.

This code can simulate the Lindbladian dynamics of a handful spins depending on the complexity of the description needed.

Second, when promising and experimentally achievable input-output relations are identified, computer simulations can be utilized to perform parameter scans of the defect-based QRC prototype envisioned or fabricated in experiments. This task can be computationally demanding; we therefore developed a C++ model of the silicon vacancy capable of simulating Lindbladian time evolution on high-performance computing (HPC) clusters. The model can automatically scan through 1,000–10,000 different parameter settings, as demonstrated by the ODMR map in Fig. 3

3.1 Mathematica model

The Wolfram Mathematica code for prototyping requires only a handful of quantities to define the system of interest. This covers all the phenomena outlined in the previous section, i.e. Hamiltonian parameters, hyperfine tensors, initial state etc. Using default settings or the specifications of the user, the Mathematica code automatically generates the Hamiltonian matrix according to Eq. (1)) (in combination with further equations incorporating fine and hyperfine structure), as well as Lindblad jump operators and an initial density matrix of compatible size. With these set the code carries out the time evolution of the system and extracts various time-dependent or time-averaged quantities of driven silicon vacancy-related systems. From the outputs, one directly infers experimental observations such as PLE, ODMR and ODNMR spectra. The capabilities of the package are exemplified in later sections.

3.2 C++ implementation for HPC

The flexibility of the Mathematica code implies numerical inefficiencies, hindering high throughput parameter scanning of point defect spin qubit systems. To remedy this shortcoming, an additional silicon vacancy model and simulator has been developed running on high-performance computing devices. The package is written in the C++ language utilizing optimized linear algebra libraries provided by the manufacturer of the selected HPC cluster. In addition, the code supports message-passing interface (MPI) parallelization over compute nodes.

Running the software requires the production of matrices, such as static and time-dependent Hamiltonians, Lindblad jump operators, the initial density matrix, and projection operators (to define output values) read in by the simulator package. To enable parameter scanning, the C++ code can read in multiples of Hamiltonian matrices, starting density, and so forth. With this it is able to scan across two parameters of the system (e.g. external magnetic field and drive frequency) simultaneously. Currently, the HPC simulator is interfaced with yet another C++ program that implements models of different silicon vacancies and provides all the necessary matrices for the simulator. In the future, the Mathematica code and possible Python packages will also be interfaced with the HPC simulator. Partners of the QRC-4-ESP project may access the HPC simulator through a cloud service. The capabilities of the high-performance computing software are demonstrated through selected examples below.

In the following, we demonstrate a nonexhaustive set of simulations of the known features of driven silicon vacancy centers in 4H-SiC. The selected numerical results detail the mechanism of the optical readout and spin initialization, which defines the

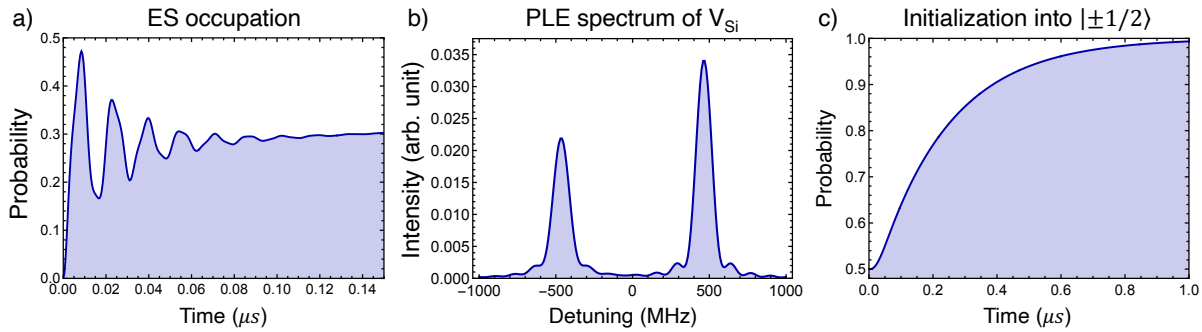

Figure 5: Response of an optically driven silicon-vacancy centre. a) Occupation of the excited state after "turning on" a strong optical drive resonant with the A_1 transition of a silicon vacancy. We observe coherent oscillation decaying with a timescale set by the lifetime of the excited state. b) Simulated photoluminescence excitation spectra of a silicon-vacancy centre in 4H-SiC. The spectrum agrees well with Fig. 2. c) Probability of finding the system in the $m_S = \pm 1/2$ spin subspace in the ground state. Due to a resonant drive of the A_2 transition and probabilistic spin non-conserving transition from $m_S = \pm 3/2$ to $m_S = \pm 1/2$, the V_{Si} centre polarizes in the $m_S = \pm 1/2$ subspace over $\sim 1\ \mu$s.

set of output parameters for QRC, as well as ground state spin dynamics subject to different driving conditions that can, for example, serve as input parameters for the system.

3.3 Coherent optical drive, photoluminescence excitation spectrum, and optical spin initialization of the VSi center

First, we examine phenomena related to resonant optical excitations of the V2 silicon vacancy centre in 4H-SiC. By applying a strong coherent drive with $\Omega = 200$ MHz^{-1} of the A2 transition ($\Delta = 470$ MHz using Eq. (1)) and extracting the probability of finding the silicon vacancy in the excited state, which is proportional to the luminescence of the centre, one can observe coherent oscillations starting at $t = 0$ and dying out within 10s of ns, see Fig. .5(a) The oscillation indicates coherent coupling between the driving field, modelled as a simple off-diagonal element in the Hamiltonian (Eq. (1) in semi-classical limit of strong, many photon electromagnetic field), and electronic states of the silicon-vacancy centre. The loss of optical coherence is dictated by the lifetime of the excited, which is 17.8 ns for the V2 centre. After the coherent oscillation has decayed, the probability of the excited state (i.e. the luminescence of the defect) slowly increases, indicating the polarization of the system bright $|m_S = \pm 1/2\rangle$ subspace.

By applying a weaker optical pumping ($\Omega = 10$ MHz) and scanning the frequency of the optical drive, i.e. scanning the Δ detuning in the rotating wave approximation, we can simulate the photoluminescence excitation spectra, exhibiting two peaks with $\approx$1 GHz spacing and asymmetric amplitudes, shown in Fig. 5(b). The two peaks correspond to transitions A1 and A2, and the experimental PLE spectrum is illustrated in Fig. **??**(a)

When comparing with measurements, one can observe that the theoretical peaks

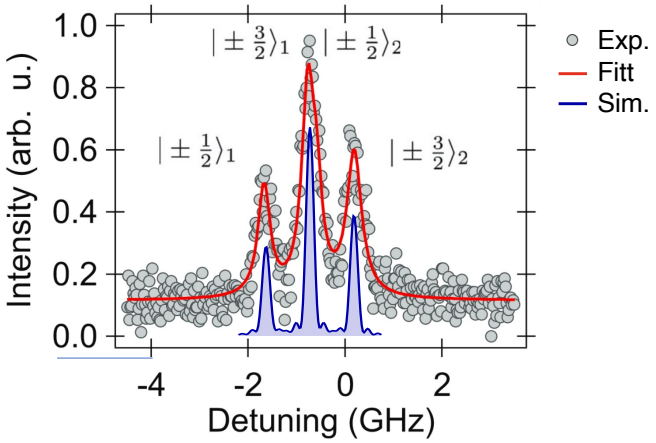

Figure 6: Comparison of theoretical and experimental PLE spectra of two V_{Si} centres with overlapping $|\pm 3/2\rangle_1$ and $|\pm 1/2\rangle_2$. The simulations omitted electric field fluctuations, causing broadening beyond the lifetime limit, and background luminescence.

are narrower/ This is due to the absence of electric field fluctuations giving rise to time-dependent detuning, and thus broadening in the experiment. The linewidth of the theoretical PLE peaks is defined by the lifetime of the states in the limit of weak optical pumping. An example of this phenomenon is shown in Fig. 6

3.4 Optically detected magnetic resonance simulation

Since the electron spin of the silicon-vacancy centre can be optically initialized and read out, one can utilize MW and RF drives to carry out electron spin and potentially nuclear spin rotations. The spin-dependent luminescence of the centers indicates resonance conditions between the spin states and the driving electromagnetic field. ODMR maps can visualize the variation of the transition energies as a function of some tunable parameters, such as the external magnetic field. In order to numerically simulate ODMR maps, we used our HPC silicon vacancy simulator and monitored the population of the $|m_S = \pm 1/2\rangle$ subspace when scanning both the frequency of the driving field and the external magnetic field.

Fig. 3 has already demonstrated the agreement between the experimental and theoretical ODMR maps, although the latter shows possible, sometimes higher-order transitions in great detail. The experimental ODMR maps can be overwhelmed by noise and hinder fine signatures of the spin dynamics of driven silicon vacancies. The signal-to-noise ratio can be enhanced by elongating the measurement time, which, can however make the recording of OMDR maps tedious work in experiments. HPC computer simulations provide a more efficient way to obtain and analyze ODMR maps. The ODMR maps provided in this report scan through a 500×500 parameter set for high-resolution imaging of the transitions.

The depth of understanding available in our simulations is exemplified by Fig. 7b) depicting a line cut, indicated by red vertical line in Fig. 7a), of the ODMR map. In addition to the broad first-order transitions and narrower double-quantum jump transitions, one can also recognize narrow peaks, and faint lines in the ODMR map, that correspond to higher-order transitions.

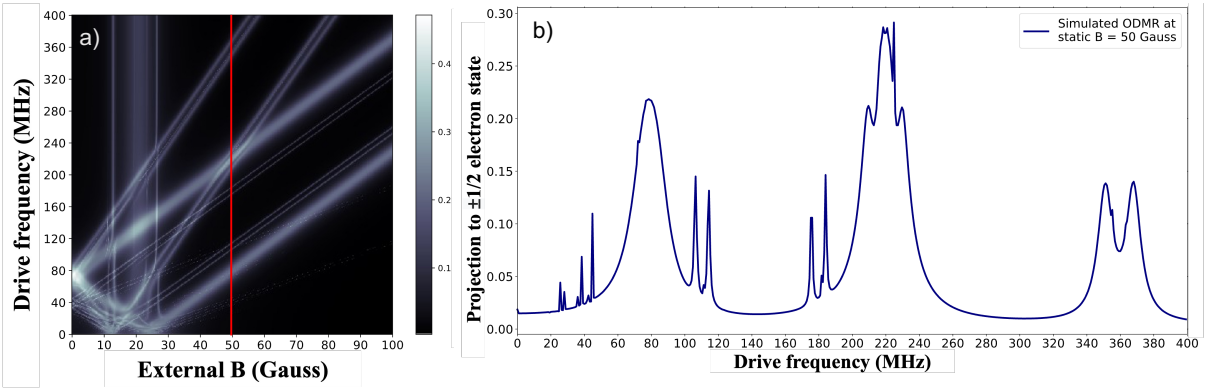

Figure 7: Continuous wave ODMR spectra of V_{Si}-^{29}Si at 50 Gauss. a) ODMR map of the system. The red vertical line indicates the line cut at a fixed magnetic field. The corresponding high-resolution ODMR spectrum is depicted in b).

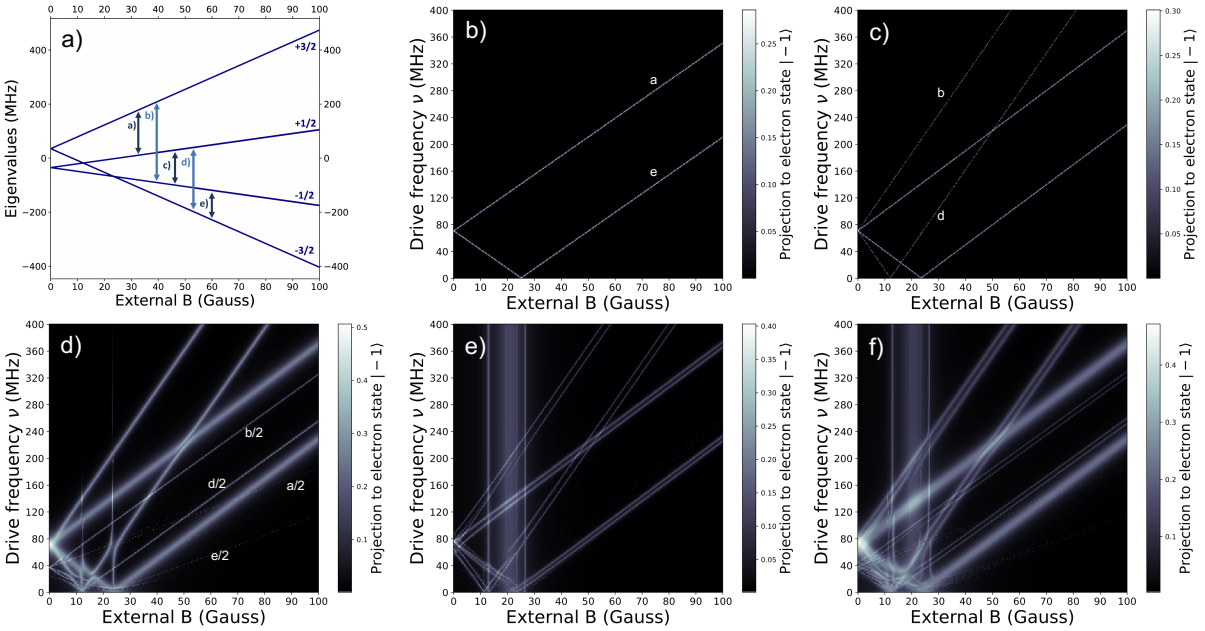

Figure 8: ODMR map as obtained by omitting different terms of the ground state spin Hamiltonian. a) energy level structure of the V2 centre as a function of the applied magnetic field highlighting relevant transition. b) weak excitation limit with linear Zeeman terms only. c) weak excitation limit with third-order Zeeman terms included. We observe double quantum jumps enabled by the term specified in Eq.(**??**). d) strong excitation limit demonstrating ME power broadening, blurring sharp lines, and two MW photon absorption giving rise to resonance lines at half energies. e) hyperfine splitting caused by a strongly coupled ($\sim$12 MHz) ^{29}Si. f) ODMR map of a strongly driven V_{Si}-^{29}Si system. Power broadening overwhelms the hyperfine splitting of the single quantum jump ODMR lines (a and e), but not the double quantum jump lines (b and d).

To understand the origin of the resonances that appear on the ODMR map and the ODMR spectrum, we can use our simulation tools to selectively turn on terms in the Hamiltonian and decorate the ODMR map, see Fig. 8. Panel (a) depicts the energy level structure of the silicon vacancy and labels single photon single and double quantum jump transitions. The ODMR map on Fig. 8(b) was obtained by including linear Zeeman term terms in addition to the zero-field splitting interaction. In Fig. 8(c) the non-linear terms were added to the Hamiltonian giving rise to new lines b and d on the ODMR map, which correspond to transitions between $|m_S = \pm 3/2\rangle \leftrightarrow |m_S = \mp 1/2\rangle$ states. Increasing the amplitude of the MW drive, one can observe a plethora of new phenomena in Fig. 8(d), including power broadening and two-MW absorption transition lines appearing at the half of the one-MW photon transition energies. Adding a second nearest neighbor nuclear spin with ≈12 MHz coupling strength one can observe the hyperfine splitting of the transition lines in Fig. 8(e) for an unpolarized nuclear spin in the limit of low MW drive. Finally, yet again increasing the amplitude of the driving MW field one can observe the merging of some of the hyperfine lines due to the power broadening, e.g. transitions a and e, while other transitions of lower coupling matrix elements, belong typically to higher order transitions preserve the hyperfine structure, see Fig. 8(f).

4 Outlook

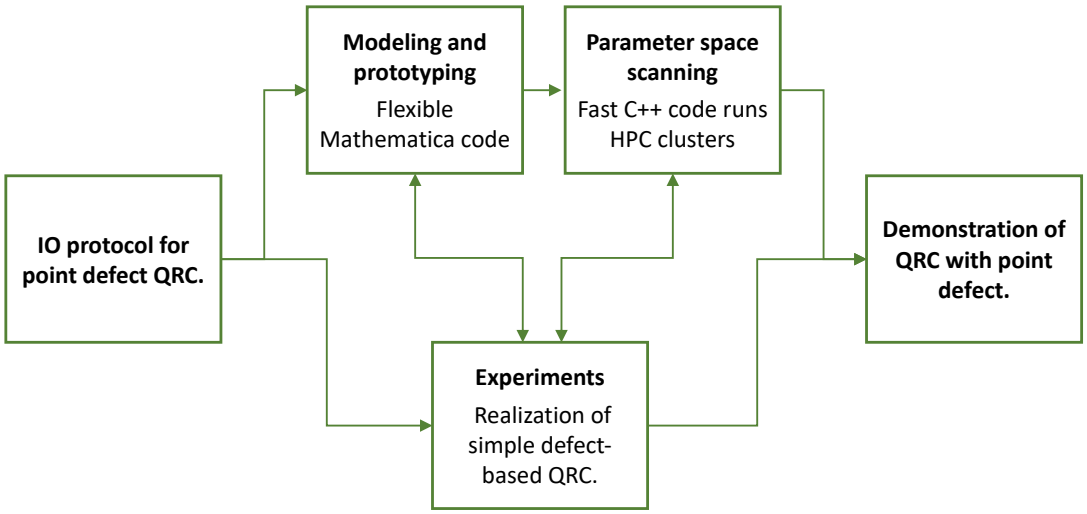

Figure 9: Workflow of demonstrating point defect-based quantum reservoir computing. The two boxes on the top summarize the role of modeling and numerical simulations. The chart depicts the connectivity of modeling to other activities of WP3 of the QRC-4-ESP project.

In this report, we have outlined the underlying physics of Silicon vacancy defects. This has informed the development both of a flexible Mathematica code for quick iteration and testing, as well as an efficient C++ code executed in a parallelised manner on HPC clusters. Using these, it has been possible to obtain quantitatively accurate simulations. These have been used to produce ODMR maps that provide high-resolution imaging, capturing higher-order transitions that .

The examples provided here are highly non-exhaustive, but the developed models have also allowed for the investigation of e.g. multi-photon absorption. Other numer-

ical investigations enabled by these codes include the claculation of PLE spectra of single and multiple silicon vacancies, coherent oscillations under strong driving, optical spin initialization, and optical dynamic nuclear polarization. These provide a vital platform for the encoding and readout of data which allows defects to act as a form of reservoir computer.

Equipped with this simulation platform, it is now possible to integrate it into the developed framework for performing reservoir computing. Using (for example) the optical drive to encode data, and performing regression on the predicted PLE, a complete pipeline for the simulation of reservoir computing tasks can be constructed. The next objective is therefore to interface the HPC and Mathematica codes with python, to enable cloud access that can facilitate direct integration. With this established, the quantitative codes outlined here can function as a modular component of the QRC pipeline. The results of this report, and their putative integration into the workflow of WP3 are schematically visualized in Fig. 9.

References

[1] Viktor Ivády, Joel Davidsson, Nguyen Tien Son, Takeshi Ohshima, Igor A. Abrikosov, and Adam Gali. Identification of Si-vacancy related room-temperature qubits in $4H$ silicon carbide. Physical Review B, 96(16):161114, October 2017. Publisher: American Physical Society.

[2] Nguyen Tien Son, Pontus Stenberg, Valdas Jokubavicius, Takeshi Ohshima, Jawad Ul Hassan, and Ivan G. Ivanov. Ligand hyperfine interactions at silicon vacancies in 4H-SiC. Journal of Physics: Condensed Matter, 31(19):195501, March 2019. Publisher: IOP Publishing.

[3] Charles Babin, Rainer Stöhr, Naoya Morioka, Tobias Linkewitz, Timo Steidl, Raphael Wörnle, Di Liu, Erik Hesselmeier, Vadim Vorobyov, Andrej Denisenko, Mario Hentschel, Christian Gobert, Patrick Berwian, Georgy V. Astakhov, Wolfgang Knolle, Sridhar Majety, Pranta Saha, Marina Radulaski, Nguyen Tien Son, Jawad Ul-Hassan, Florian Kaiser, and Jörg Wrachtrup. Fabrication and nanophotonic waveguide integration of silicon carbide colour centres with preserved spin-optical coherence. Nature Materials, 21(1):67–73, January 2022. Bandiera_abtest: a Cg_type: Nature Research Journals Number: 1 Primary_atype: Research Publisher: Nature Publishing Group Subject_term: Quantum information;Quantum physics;Single photons and quantum effects Subject_term_id: quantum-information;quantum-physics;single-photons-and-quantum-effects.

[4] Di Liu, Florian Kaiser, Vladislav Bushmakin, Erik Hesselmeier, Timo Steidl, Takeshi Ohshima, Nguyen Tien Son, Jawad Ul-Hassan, Öney O. Soykal, and Jörg Wrachtrup. The silicon vacancy centers in SiC: determination of intrinsic spin dynamics for integrated quantum photonics. npj Quantum Information, 10(1):1–9, July 2024. Publisher: Nature Publishing Group.

[5] D. Simin, V.A. Soltamov, A.V. Poshakinskiy, A.N. Anisimov, R.A. Babunts, D.O. Tolmachev, E.N. Mokhov, M. Trupke, S.A. Tarasenko, A. Sperlich, P.G. Baranov, V. Dyakonov, and G.V. Astakhov. All-Optical dc Nanotesla Magnetometry Using Silicon Vacancy Fine Structure in Isotopically Purified Silicon Carbide. Physical Review X, 6(3):031014, July 2016.

[6] Krisztián Szász, Tamás Hornos, Martijn Marsman, and Adam Gali. Hyperfine coupling of point defects in semiconductors by hybrid density functional calculations: The role of core spin polarization. Physical Review B, 88(7):075202, August 2013. Publisher: American Physical Society.

[7] István Takács and Viktor Ivády. Accurate hyperfine tensors for solid state quantum applications: case of the NV center in diamond. Communications Physics, 7(1):1–6, June 2024. Publisher: Nature Publishing Group.